HHS Public Access

Author manuscript

Phys Med Biol. Author manuscript; available in PMC 2022 May 17.

Published in final edited form as:

Phys Med Biol. ; 64(9): 095022. doi:10.1088/1361-6560/ab1456.

Atlas-based automatic planning and 3D–2D fluoroscopic guidance in pelvic trauma surgery

R Han[1], **A Uneri**[1], **T De Silva**[1], **M Ketcha**[1], **J Goerres**[1], **S Vogt**[2], **G Kleinszig**[2], **G Osgood**[3], **J H Siewerdsen**[1,4]

[1]Department of Biomedical Engineering, The Johns Hopkins University, Baltimore, MD, United States of America

[2]Siemens Healthineers, Erlangen, Germany

[3]Department of Orthopaedic Surgery, The Johns Hopkins Hospital, Baltimore, MD, United States of America

[4]Department of Biomedical Engineering, Johns Hopkins University, Traylor Building, Room 622, 720 Rutland Avenue, Baltimore, MD 21205, United States of America

Abstract

Percutaneous screw fixation in pelvic trauma surgery is a challenging procedure that often requires long fluoroscopic exposure times and trial-and-error insertion attempts along narrow bone corridors of the pelvis. We report a method to automatically plan surgical trajectories using preoperative CT and assist device placement by augmenting the fluoroscopic scene with planned trajectories.

A pelvic shape atlas was formed from 40 CT images and used to construct a statistical shape model (SSM). Each member of the atlas included expert definition of volumetric regions representing safe trajectory within bone corridors for fixating 10 common fracture patterns. Patient-specific planning is obtained by mapping the SSM to the (un-segmented) patient CT via active shape model (ASM) registration and free-form deformation (FFD), and the resulting transformation is used to transfer the atlas trajectory volumes to the patient CT. Fluoroscopic images acquired during K-wire placement are in turn augmented with projection of the planned trajectories via 3D–2D registration. Registration performance was evaluated via leave-one-out cross-validation over the 40-member atlas, computing the root mean square error (RMSE) in pelvic surface alignment (volumetric registration error), the positive predicted value (PPV) of volumetric trajectories within bone corridors (safety of the automatically planned trajectories), and the distance between trajectories within the planned volume and the bone cortex (absence of breach). A cadaver study was conducted in which K-wires were placed under fluoroscopic guidance to validate 3D–2D registration accuracy and evaluate the potential utility of augmented fluoroscopy with planned trajectories.

The leave-one-out cross-validation achieved surface RMSE of 2.2 ± 0.3 mm after ASM registration and 1.8 ± 0.2 mm after FFD refinement. Automatically determined surgical plans conformed within bone corridors with PPV > 90% and centerline trajectory within 3–5 mm

jeff.siewerdsen@jhu.edu .

of the bone cortex. 3D–2D registration in the cadaver study achieved 0.3 ± 0.8 mm accuracy (in-plane translation) and <4° accuracy (in-plane rotation). Fluoroscopic images augmented with planning data exhibited >90% conformance of volumetric planning data overlay within bone, and all centerline trajectories were within safe corridors.

The approach yields a method for both automatic planning of pelvic fracture fixation and augmentation of fluoroscopy for improved surgical precision and safety. The method does not require segmentation of the patient CT, operates without additional hardware (e.g. tracking systems), and is consistent with common workflow in fluoroscopically guided procedures. The approach has the potential to reduce operating time and radiation dose by minimizing trial-and-error attempts in percutaneous screw placement.

Keywords

atlas-based registration; 3D–2D registration; active shape model; pelvic trauma; surgical planning; surgical guidance

1. Introduction

Pelvic fractures resulting from trauma present a challenge even to experienced surgeons in accurately placing instrumentation within the complex 3D anatomy of the pelvis and carry a high rate of mortality (8.3%) (Yoshihara and Yoneoka 2014). Percutaneous fracture fixation is a prevalent means to stabilize minimally displaced fractures, involving the insertion of K-wires along narrow bone corridors with subsequent placement of cannulated screws. During surgery, a mobile C-arm is commonly used to acquire fluoroscopic images incrementally during K-wire and screw insertion to visualize the position of surgical devices with respect to bone anatomy in real time. Owing to the challenge of cognitive reckoning of 3D pelvic morphology within the 2D fluoroscopic scene, accurate K-wire placement carries a considerable learning curve, and even experienced surgeons often resort to trial-and-error and extended fluoroscopy runtimes (exceeding 120 s total (Gras et al 2010)). In this work, we report a method to augment the fluoroscopic scene with automatically determined ‘acceptance corridors’ corresponding to safe bone corridors for K-wire insertion. Such augmentation could help reduce trial-and-error attempts in navigating instruments within complex 3D anatomy as depicted in 2D x-ray images and reduce radiation exposure to the patient and operating staff, which is a growing area of concern in the orthopaedic surgery community (Buls et al 2003, Lee et al 2012, Loisel et al 2017).

Preoperative CT is routinely used to assess pelvis fracture and complex 3D bone morphology in proximity to adjacent nerves and vessels. However, stereotactic navigation using the preoperative CT is rare, due in part to the additional cost, equipment, and workflow associated with such systems, leaving real-time fluoroscopic guidance as the common clinical standard. Previous studies have utilized the preoperative CT to provide patient-specific pelvic shapes by incorporating prior knowledge of anatomical shape to delineate a patient-specific model within the (unsegmented) patient image. A widely-studied approach for atlas-based soft-tissue segmentation is by direct deformable registration between atlas images and the patient image (Lorenzo-Valdés et al 2002, Aljabar et al 2009,

Isgum et al 2009), in which a volumetric soft-tissue structure annotation (e.g. brain) is propagated from the atlas members to the patient image and combined to generate a final voxelwise segmentation. Such an approach exercises the entire volumetric image content in solving the transformation, but it is computationally expensive. For purposes of orthopaedic trauma planning (involving high-contrast structures such as the pelvis) a surface-based approach is more computationally efficient and well suited to the pertinent image data and task.

Another common approach for shape segmentations is active shape model (ASM) (Cootes et al 1994) that uses the principal components of an shape atlas as statistical model, and several studies (Lamecker et al 2004, Ellingsen et al 2010) have used ASM for pelvis segmentation in CT. Using the principal components alone in ASM is subject to segmentation error when the patient anatomy is not well represented in the atlas. Several previously reported methods have combined PCA with free-form deformation (FFD) to improve performance. (Zhang et al 2013, Ren et al 2014) combined PCA with FFD for deformation model estimation and updated CT images from *a prior* based on limited-angle x-ray projections. Seim et al (2008) combined ASM with a constrained FFD for more robust segmentation of the liver using graph-cut optimization.

The patient-specific pelvic shape reflected in preoperative images provides a basis for anatomical trajectories for screw fixation (Giannoudis et al 2007, Bishop and Routt 2012). Depending on the forces exerted during trauma and the pelvic biomechanics, common trajectories for pelvic fracture fixation include: (1) anterior column to iliac crest (Giannoudis et al 2007); (2) posterior column (Starr et al 1998); (3) anterior column along the superior pubic ramus (Routt et al 1995); (4) anterior inferior iliac spine (AIIS) to posterior superior iliac spine (PSIS) (Schildhauer et al 2002); and (5) iliosacral screws joining the ilium and sacrum at S1 and S2 (Routt et al 1995). Using manual or semiautomatic segmentation of bone surfaces, (Knez et al 2016) and (Goerres et al 2017a) proposed methods for planning of spinal pedicle screws, and (Banerjee et al 2016) proposed planning of acetabular screws. Recent work (Goerres et al 2017b) utilized ASM registration of the pelvis for automatic determination of screw trajectories, helping to resolve the bottleneck of manual trajectory planning that can be prohibitive within the rapid workflow of trauma surgery.

In this work, we extend the method of Goerres et al (2017b) for more accurate, segmentation-free registration, surgical planning, and guidance. Previous work (Goerres et al (2017b) used an atlas of 12 single-sided female hip bones and 3 relevant trajectories (superior pubic ramus, AIIS to PSIS, and posterior column). The current work expands the atlas to 40 bilateral pelves with sacrum for both male and female subjects with ten relevant trajectories (bilateral superior pubic ramus, bilateral AIIS to PSIS, bilateral posterior column, bilateral anterior column to iliac, and iliosacral trajectories at levels S1 and S2). Moreover, the atlas of pelvic shapes and reference trajectories is made available in the public domain. The current work also improves the accuracy of atlas-to-image registration by incorporating an unconstrained FFD stage. Trajectories are defined volumetrically (see, linear trajectories as in Goerres et al (2017a)) to include all acceptable orientations of each trajectory within safe bone margins and mitigate bias associated with a simple linear trajectory.

Previous work (Goerres et al 2017b) proposed a 3D guidance framework to localize an implant (viz., K-wire) in 3D CT by 3D–2D registration computed between CT and multiple radiographs. In the current work, we present a method to augment the fluoroscopic scene directly with the acceptance corridors for a given implant trajectory via 3D–2D registration between CT and a single radiograph. Whereas Goerres et al (2017b) used gradient correlation as a similarity metric for registration, the work below employs gradient orientation (GO) for improved robustness in the presence of content mismatch between the CT and radiograph. The resulting single-shot augmented fluoroscopy method provides more streamlined workflow that is likely more consistent with the rapid workflow requirements of orthopaedic surgery. It also renders the augmentation directly in the fluoroscopic scene—a more familiar image context in trauma surgery compared to orthogonal tomographic slices in 3D navigation. This form of augmented fluoroscopic guidance has an acceptable time latency and provides near real time feedback for each radiograph acquired during implant insertion without interrupting clinical workflow. By presenting such safety corridors in multiple views (e.g. commonly acquired inlet, outlet, anterior–posterior [AP], and lateral [LAT] views), such augmentation is anticipated to facilitate accurate reckoning of the 3D device orientation within the pelvis and improve understanding of the trajectory of the device within the complex 3D morphology of the pelvis.

2. Methods

Figure 1 illustrates the process for automatic planning of percutaneous pelvic screws and visualization of planned trajectory under fluoroscopic guidance using atlas-to-image: preoperatively, an atlas of pelvis shapes and reference trajectories is registered to the patient CT via ASM, and patient-specific trajectories are automatically determined using the ASM transformation without the need for manual segmentation or annotation of the CT; intraoperatively, the preoperative CT is mapped to intraoperative fluoroscopy via 3D–2D registration by matching digitally reconstructed radiograph (DRR) to x-ray image, and trajectory plans are overlaid on the x-ray image to provide 2D fluoroscopic guidance. The system thereby provides guidance analogous to surgical navigation—specifically, helping the surgeon to determine if instrument trajectories are within acceptance corridors—without additional tracking systems. By augmenting each fluoroscopic view with the acceptance corridor (green overlay in figure 1), and with direct visualization of whether the instrument (e.g. K-wire) is within an acceptance corridor in multiple views, the system could help to resolve uncertainty in 3D positioning within the complex anatomical shape and thereby reduce trial-and-error, radiation exposure, and operating time.

2.1. Trajectory planning

2.1.1. Pelvis shape and trajectory atlas—A pelvis atlas was created from CT images drawn from the Cancer Imaging Archive (Clark et al 2013, Roth et al 2014, Seff et al 2014). A total of $n = 40$ pelves (20 male and 20 female; age 18–68 years (median 46.5)) were included. The range reflects a better spectrum of pelvic morphology associated with gender, age, and body habitus than previous work (Goerres et al 2017b). The CT images were processed to volume size of 512 × 512 × 500 voxels with voxel size ranging from 0.63 × 0.63 × 1.00 mm^3 to 0.98 × 0.98 × 1.25 mm^3. Each CT image was manually segmented

by a research assistant trained in basic pelvic anatomy. The left pelvis, right pelvis, and sacrum were individually segmented. Manual segmentation was performed slice-by-slice in axial planes using the Medical Imaging Interaction Toolkit (German Cancer Research Center, Heidelberg Germany), and a built-in smoothing filter was applied to smooth the manual contours. A selection of segmentations was repeated four times to evaluate the intra-observer reproducibility, which showed an overlap Dice coefficient of 0.93 ± 0.01. For the sacrum, only the first three levels (S1–S3) were segmented, since those were the levels relevant to iliosacral screw trajectories, and because the lower levels and coccyx were seen to exhibit very broad morphological variations. Each segmentation was converted to a closed, triangulated surface mesh S_i, $i \in (1, \ldots, n\}$ with 5000 equidistant vertices.

Generation of the pelvic statistical atlas generally followed the method of (Goerres et al 2017a). A statistical shape model (SSM) describing the variations in shape among atlas members was constructed using principal component analysis (PCA). One surface was randomly chosen as a template surface and was deformably registered to all remaining 39 surfaces via coherent point drift (CPD) (Myronenko and Song 2010). This process provided surface representation for each atlas member that shared corresponding vertices between each atlas member and the template surface. Since each deformably registered surface was defined in its own CT coordinate, a generalized procrustes analysis (GPA) was applied to rigidly align the surfaces into the template coordinate space. The vertex coordinates for each surface were then concatenated into a vector, such that

$$\boldsymbol{x_i} = (x_1, y_1, z_1, \ldots, x_n, y_n, z_n)^T \tag{1}$$

and PCA was applied to the surface vectors by computing the mean shape $\bar{x}$ and the eigenvectors corresponding to the largest k eigenvalues λ_i retained in a matrix $P \in \mathbb{R}^{3n \times k}$. A given surface can then be approximated by the SSM with a principal weight vector $b \in \mathbb{R}^{k \times 1}$:

$$\boldsymbol{x_i} = \bar{\boldsymbol{x}} + \boldsymbol{P}b_i\,. \tag{2}$$

An important addition to the atlas beyond descriptors of pelvic shape is the inclusion of volumetric regions corresponding to acceptable regions for device placement in ten common screw trajectories in pelvic trauma—as mentioned above: (left and right) AIIS to PSIS; (left and right) superior pubic ramus; (left and right) anterior column to iliac crest; (left and right) posterior column; and iliosacral trajectories (at levels S1 and S2). Reference trajectories were manually defined to include all possible orientations in the desired bone corridors. As shown in figure 2, standard trajectory entry surfaces (in both antegrade and retrograde manner) were manually annotated and dilated on the pelvic segmentation mesh to cover each set of possible entry locations. Points on the two surfaces were connected with a cylinder of 1.6 mm radius (the radius of a standard percutaneous K-wire). If the cylinder was entirely contained in the closed bone surface, the voxels of the cylinder were included in the acceptance corridor, denoted C_i. A hole filling operation was then applied, and a triangulated mesh representation of the trajectory acceptance corridor was created with 500 equidistant vertices, denoted S_{Ci}.

The atlas—including CT images, pelvic segmentations, shape model, and reference trajectories—are available in the public domain and can be downloaded from: https://istar.jhu.edu/downloads/. In addition to the inclusion of reference trajectories, the atlas adds to the body of previously reported open science atlases (Lamecker et al 2004, Seim et al 2008, Ellingsen et al 2010, Zhang et al 2016), uses commonly available data formats, does not require other custom software, and represents complete scans covering the pelvis from iliac crest to ischium.

2.1.2. Atlas-to-image registration—The pelvic shape atlas was registered to CT using ASM to obtain a surface representation of patient-specific pelvic shape. The resulting pelvis surface $\boldsymbol{y}$ is parametrized by a rigid transformation T_{ASM} and a weight vector b_{ASM} of the principal components matrix P:

$$\boldsymbol{y} = T_{\mathrm{ASM}}(\bar{\boldsymbol{x}} + Pb_{\mathrm{ASM}}). \tag{3}$$

ASM parameters are solved iteratively by locally estimating the displacement of vertices $\Delta \boldsymbol{y_p}$ based on image content and globally fitting the surface with the SSM constraints by estimating a rigid pose/scale change T_{ASM} and a PCA weight b_{ASM}. $\Delta \boldsymbol{y_p}$ was determined by moving vertices to the locations of highest image gradient magnitude along their shape normal. To maintain robustness to noise in the image gradient, a random sample consensus (RANSAC) algorithm was applied as describe in Goerres et al (2017a). A subset of vertices ($n = 100$) denoted by RANSAC ($\boldsymbol{y}$) was randomly selected as input to rigid registration and the resulting transformation was applied to the full surface to obtain the sum of gradient magnitudes Σ_y for all vertices:

$$\hat{T}_{\mathrm{ASM}}^{(i)} = \arg\min_{T} \left\| T(\mathrm{RANSAC}(\boldsymbol{y})) - (\mathrm{RANSAC}(\boldsymbol{y} + \Delta\, y_p)) \right\|^2 \tag{4a}$$

$$\Sigma_y^{(i)} = \int_{v \in y} \left| \nabla I\left(\hat{T}_{\mathrm{ASM}}^{(i)}(v)\right) \right| dv \tag{4b}$$

where the two RANSAC() are the same randomly selected subset, and $|\nabla I(\cdot)|$ is the image gradient magnitude. This process is repeated for 50 times, and the transform with the highest Σ_y is taken as the update $\hat{T}_{\mathrm{ASM}}$. The weight vector was then updated by projecting the residual displacement $\Delta \boldsymbol{y_s} = \boldsymbol{y} + \Delta \boldsymbol{y_p} - T_{\mathrm{ASM}}$ ($\boldsymbol{y}$ to the atlas SSM:

$$\Delta\, b_{\mathrm{ASM}} = P^{-1} \hat{T}_{\mathrm{ASM}}^{-1}(\Delta\, \boldsymbol{y_s}). \tag{5}$$

The estimate of vertex displacement can be prone to errors arising from adjacent bones (e.g. latching to a nearby surface at the femoral head or L5 vertebra), image noise, and image artifacts. The ASM framework was therefore applied in a multi-scale hierarchy—starting from coarsely sampled volumes (to improve speed and inhibit the surface from latching to nearby structures) and proceeding to progressively finer sampling (to improve robustness

to noise and adjacent anatomical content) as in Cootes et al (1994). Another variable in the multiresolution pyramid was the number of principal components (P in equation (5)) which was varied to allow the ASM to adjust the most significant modes of variation before tuning the minor modes. The multiresolution schedule is detailed in table 1 with isotropic downsampling [4×, 2×, 1×], Gaussian smoothing kernel width (voxels) [4, 2, 1], and number of principal components [2, 4, 8, 12]. The search spacing δ was set to 1 voxel at each image resolution level. At each pyramid level, the convergence criterion was set by the mean displacement vector magnitude $\overline{|\Delta \boldsymbol{y}_p|}$ falling below a particular threshold (set to 0.5δ in the current work). Isotropic image downsampling was evaluated at powers of 2, [1×, 2×, 4×, 8×, 16×, …]. Beyond 8 × downsampling, bone gradients were no longer salient, and some narrower regions of the pelvis shape were no longer visible. Gaussian kernel widths in the range of [0, 1, 2, 4] voxels were evaluated for each downsampling factor, and the kernel width matching the downsampling factor resulted in best registration accuracy. Reducing the Gaussian kernel width led to noisy gradient computation and instability in the registration process, and increasing the kernel width well beyond the nominal value smoothed out useful gradients and made bone edges hard to localize. The maximum number of principal components was determined by computing the cumulative variance, and in the pelvis SSM, the first 12 principal components constituted more than 90% of the total variance. Using even more principal components increased the dimensionality of the PCA projection operation in equation (5) without improving registration accuracy (and could lead to errors in estimation of the weight vector, b).

Although ASM is robust in surface-to-image registration, the shapes obtained from ASM are constrained by the space spanned by principal components of the atlas. If a particular patient's pelvis shape is not well represented in the SSM principal component space, ASM tends to be less accurate and does not to converge to the correct solution. Therefore, a refinement to the basic ASM method was incorporated in which FFD was used after ASM to achieve better local convergence. The FFD step iteratively solved for vertex displacements along surface normals without principal component constraints. Instead of maximizing the image gradient magnitude, the FFD step maximized a directional image gradient along the surface normal $\boldsymbol{n}_v$ of each vertex v to avoid latching to nearby structures $\nabla I(v) \cdot \boldsymbol{n}_v$. Since FFD can suffer from image noise and artifacts, a sinc smoothing function with passband at 10% of Nyquist frequency was applied to the registered surface after every FFD iteration. The sinc filter helped to evenly distribute and smooth the displacements of adjacent vertices for accurate local shape representation.

2.1.3. Automatic trajectory planning—The registration method discussed in the previous section yields a sparse displacement field from surfaces of the atlas to image gradients in the patient CT, which can in turn be used to deform the reference trajectory volumetric meshes to the patient CT coordinates and thereby produce patient-specific trajectories as illustrated in figure 3 for the AIIS to PSIS trajectory. There are a variety of ways to transform the trajectory atlas to patient coordinates: for pedicle screw placement in spine surgery, (Knez et al 2016) determined the entry points and poses of screw trajectories from entry surfaces on the vertebral body; and Goerres et al (2017a) deformed a trans-pedicle reference trajectory from each atlas member to the patient registration. For pelvic

trauma screw trajectories in this work, we consider a full volumetric description of each trajectory in the atlas, thus accounting for morphological differences between the patient pelvis and the atlas (such as narrowing of superior ramus or increased curvature of the sacrum). In addition, compared to a single trajectory, the volumetric trajectory atlas includes all safe (i.e. non-breaching) trajectory poses.

The mean value coordinates (MVC) method (Ju et al 2005) was used to interpolate the displacement at every vertex of the trajectory surface based on mean value transformation between atlas surface $\boldsymbol{x_i}$ and registered surface $\boldsymbol{y}$. Each trajectory surface S_{C_i} is mapped to $\widetilde{S}_{C_i}$ in the CT image space and voxelized to a binary volume $\widetilde{C}_i$. A total accumulation map A_c is computed by taking the normalized sum of the mapped trajectory volumes $\widetilde{C}_i$, $i \in \{1, \ldots, n\}$. The accumulation map provides a confidence measure of screw trajectories, where values closer to 1 indicate greater consensus of the atlas. Compared to the use of a single atlas member (e.g. that giving closest match to the estimate), computing the trajectory volume according to the accumulation of all atlas members has potential advantages, including: (1) incorporating cross-subject anatomical variations into trajectory planning; and (2) robustness to surface registration error and bias toward a single atlas member.

2.2. Application to fluoroscopic guidance

2.2.1. Image-to-radiograph 3D–2D patient registration.—Fluoroscopy images acquired during surgery can be registered to preoperative CT using 3D–2D registration—for example, previous work using 3D–2D registration for labeling of vertebrae (Otake et al 2013, De Silva et al 2016). As shown in the lower branch of figure 1, the 3D–2D registration is performed by optimizing image similarity between DRRs and one or more fluoroscopy images R_θ in a rigid 6 degree-of-freedom (DOF) transformation space, T_{CT}. In this work, GO was used as a similarity metric (De Silva et al 2016), which has been shown to be more robust against the presence of surgical implants in the fluoroscopic image (e.g. K-wires and percutaneous screws that may be absent from the preoperative CT):

$$\mathrm{GO}\,(I_1, I_2) = \frac{1}{\max\,(N, N_{\mathrm{LB}})} \sum_{i \in \{\,\Omega\,:\,|\nabla I_1(i)| > t_1 \cap |\nabla I_2| > t_2\}} w'(i) \tag{6a}$$

$$w'(i) = \frac{2 - \ln\,(|\psi_i| + 1)}{2} \tag{6b}$$

where ∇ denotes the gradient operator, ψ_i denotes the angle between two gradient vectors at pixel location i, and N and N_{LB} denote the number of evaluated pixels and a lower bound of half of the total pixels in the radiograph, respectively. The thresholds t_1 and t_2 are defined as the median gradient magnitude of each image, such that only pixels with gradient magnitude exceeding the thresholds are evaluated. The DRR is computed for a given gantry pose, θ, by integrating along rays, r_θ, through the transformed CT volume, $T(V_{\mathrm{CT}})$, and the line integrals are discretized using trilinear voxel interpolation of the volume. The transformation that maximizes GO between the DRR and fluoroscopic image R_θ:

$$\hat{T} = \underset{T}{\operatorname{argmax}} \mathrm{GO}\left(R_\theta, \int_{r_\theta} T(V_{\mathrm{CT}}) dr_\theta \right) \tag{7}$$

defined the 3D–2D registration, which was solved using the covariance matrix adaption evolution strategy (CMA-ES) optimization algorithm (Hansen et al 2003). The CMA-ES method generates a population of random sample points around the current estimate following a multivariate normal distribution, and each sample point evaluation can be computed in parallel. In this work, a population size of 200 was used, and the initial standard deviation was set to σ = 15 mm and 15°, respectively: The 3D–2D registration algorithm was implemented on GPU to parallelize computation and achieve runtimes suitable to practical application, with average registration runtime of 12.8 s in the cadaver studies below.

2.2.2. Augmented fluoroscopic guidance—Figure 4(a) illustrates the challenge of assessing the 3D orientation of K-wires with respect to safe bone corridors within the fairly complex 3D pelvic anatomy projected onto a 2D plane. Besides limited depth resolution, overlaying structures present a complex radiographic scene in which it can be difficult to determine orientation. The automatic determination of acceptable device trajectory within the fluoroscopic view provides additional information for guidance and decision support—particularly in complex scenes and when applied to 2 or more fluoroscopic views, thereby resolving the question of depth.

As the accumulation map A_{c} is defined in the same coordinate space as the preoperative CT, its relation to each radiograph is readily provided by 3D–2D registration (section 2.2.1) with no additional computation. Figure 4(c) shows two example acceptance trajectories (denoted $P_{A\mathrm{c}}$) computed by projecting the 3D accumulation map onto the fluoroscopic image:

$$P_{A_{\mathrm{c}}} = \int_{r_\theta} \hat{T}(A_{\mathrm{c}}) dr_\theta \,. \tag{8}$$

In addition to 2D fluoroscopic augmentation, the method is applicable to 3D navigation via the acquisition of two or more fluoroscopic views. In 3D navigation, the 3D–2D registration must solve for both the anatomy (as described above) as well as the K-wire—i.e. automatically detect the instrument and compute its 3D pose. Previous work by Goerres et al (2017a) used deformable known component 3D–2D registration to determine the pose and orientation of K-wires and screws with three radiographs separated by at least 20° from each other. The automatic planning and 2D fluoroscopic guidance system investigated in this work is thus extensible to 3D guidance with minimal interference to workflow.

2.3. Experiments

2.3.1. Accuracy of trajectory planning: atlas cross-validation—The atlas registration and trajectory planning method (section 2.1) was evaluated in a leave-one-out cross-validation of the atlas. For each member of the atlas, the corresponding CT image was

used as the patient image, and the remaining images were used for constructing an atlas [$(n-1)$ members]. The atlas-to-image registration accuracy was measured by the Euclidean surface distance between the registered surface y and the manual segmentation surface S_{ref}, which was computed by the surface root mean square error (RMSE) between every vertex v on y to its closest vertex on S_{ref}:

$$d_{\text{rms}}(y, S_{\text{ref}}) = \sqrt{\frac{1}{|y|}\int_{v \in y}\left(\min_{s \in S_{\text{ref}}} |v - s|\right)^2 dv} \tag{9}$$

where $|y|$ is the number of vertices in the surface y.

The automatically determined trajectory volumes were evaluated both in terms of the accuracy of the accumulation volume and the conformance of the optimal trajectory within the accumulation volume. The accuracy of the accumulation volume was quantified in terms of the positive predictive value (PPV) for values of the accumulation volume above 0.5 (indicating consensus by over half of the atlas) in comparison to reference defined by manual pelvis segmentation:

$$\text{PPV}_{A_c} = \frac{(A_c > 0.5) \cap A_{\text{ref}}}{A_c > 0.5}. \tag{10}$$

The PPV gives the probability that a voxel within the accumulation map is truly within an acceptable corridor. Based on the accumulation volume, an optimal straight-line trajectory was determined by fitting a straight, rigid cylinder to the accumulation map between the two entry/exit surfaces in the coordinate system of the patient CT. The acceptability of the resulting trajectory was measured by sampling equidistant points $t^{(i)}$, $i \in \{1, \ldots, n_t\}$ along the trajectory and calculating the distance from each sample to the cortical bone surface $\min_{s \in S_{ref}} |t^{(i)} - s|$. Distance values greater than zero indicate that the trajectory is within the bone corridor, and negative values indicate breach of the bone cortex.

The sensitivity of automatic trajectory planning to the accuracy of atlas-to-image registration was investigated by stopping the registration at iterations prior to convergence and analyzing the conformance (PPV) of the resulting trajectory. The superior pubic ramus and iliosacral S1 trajectories were chosen as challenging examples among the ten trajectories. The multiresolution registration schedule described in table 1 was used, and trajectory conformance was analyzed for the registration stopped at the Initialization, 4×, 2×, 1×, and FFD steps.

2.3.2. Pre-clinical studies in cadaver—The performance of atlas registration, accuracy of trajectory planning, and potential benefit of augmented fluoroscopic guidance was further evaluated in a study involving placement of four K-wires in a fresh human cadaver. The specimen was acquired from the Maryland Anatomy Board and used under approved state and institutional protocols. The four K-wire trajectories corresponded to the following pelvic trajectories: AIIS to PSIS, anterior column to iliac crest (left), superior

ramus (left), and iliosacral (at S1). An intraoperative CBCT scan (O-arm, Medtronic, Littleton MA) was acquired with the cadaver in prone position prior to K-wire placement, providing the basis for atlas-to-image registration and trajectory planning (section 2.3.1). The CBCT image was reconstructed at 0.42 × 0.42 × 0.42 mm^3 with a volume size of 880 × 512 × 568 voxels. A fellowship-trained orthopaedic surgeon inserted four K-wires (Stryker, Kalamazoo MI) of 1.6 mm radius. The superior ramus K-wire was slightly misplaced on purpose to demonstrate the potential benefit of fluoroscopic guidance in depicting breaches that can be difficult to appreciate in 2D projections alone. In placing each K-wire, fluoroscopic images were acquired (also on the O-arm) at three stages of insertion in views that are common to trauma surgery (viz., the posterior-anterior (PA), LAT, outlet, and inlet views). A total of (4 K-wires) × (3 stages) × (4 views) = 48 radiographs were acquired and 3D–2D registration was computed for each view.

3D–2D registration accuracy (CBCT to single fluoroscopy images) was evaluated in terms of the accuracy of the transformation T_{CT} and projection distance error (PDE). The error in each of the 6-DOF geometric parameters (x, y, z, α, β, γ) was computed, with the x and y axes defined as parallel to the detector edge and the z axis defined by their cross product (depth direction out of the radiographic plane). Similarly, the α, β, γ parameters defined the orientation of the transformation in the zyx Euler angle representation. Up to 10 unambiguous anatomical landmarks were identified in CBCT and radiographs, and PDE was measured as the distance (in the projection domain) between the registered landmarks in DRRs and the landmarks on radiographs:

$$\mathrm{PDE} = \frac{1}{N}\sum_{i=1}^{N}\left\| p_i^{\mathrm{DRR}} - p_i^{\mathrm{radiograph}} \right\| \tag{11}$$

where $p_{\mathrm{i}}^{\mathrm{DRR}}$ is the projection of the ith target point on preoperative CT projected by the registration transformation, and $p_{\mathrm{i}}^{\mathrm{radiograph}}$ is the ith target point on the fluoroscopy image. The accuracy of augmented fluoroscopic guidance was evaluated by calculating the PPV of the projected trajectory accumulation in terms of truth defined by the reference trajectory corridors:

$$PPV_{\mathrm{P}} = \frac{\left(P_{A_{\mathrm{c}}} > 0.5\right) \cap P_{A_{\mathrm{ref}}}}{P_{A_{\mathrm{c}}} > 0.5} \tag{12}$$

where $P_{A_{\mathrm{c}}}$ is the normalized projected trajectory accumulation, and $P_{A_{\mathrm{ref}}}$ is the reference trajectory corridor (in the projection domain on the radiograph).

3. Results

3.1. Accuracy of atlas-to-image registration

Leave-one-out cross-validation of atlas registration among 40 pelves showed median surface distance error of 2.2 mm RMSE (0.3 mm interquartile range [IQR]) following ASM

registration. Figure 5(a) plots the surface RMSE following each step in the multiresolution pyramid, showing a decrease in surface RMSE at each level. The FFD step further reduced surface RMSE to median 1.8 mm (0.2 mm IQR), showing a statistically significant reduction compared to ASM registration at the same image resolution (Student t-test $p \ll 0.05$).

The same multiresolution pyramid was applied to registration to CT images of the cadaver, yielding surface RMSE of 2.2 mm (0.9 mm IQR) after ASM registration and 1.6 mm (0.5 mm IQR) after FFD. Figures 5(b)–(d) illustrates the registration accuracy, with line contour overlays depicting the registered pelvis surface on the CT image. A 3D rendering of registration error at every vertex on the surface is shown in Figure 5(e), demonstrating fairly uniform registration (~1 mm surface RMSE) across most of the pelvis, with larger registration error in locations of high curvature and shape variations, such as the edges of the iliac crest, pubic symphysis, and the AIIS. For purpose of pelvic fracture fixation, however, the paths of percutaneous fixation trajectories tend to traverse areas such as the body of the ramus and iliac wings, which show error within ~1 mm. Moreover, as shown below, there is a degree of intrinsic robustness in the trajectory planning method in that the trajectories (including an effective interpolation by MVC) are not strongly perturbed by localized surface registration errors.

3.2. Accuracy of trajectory planning

The accuracy of planned trajectories was evaluated in leave-one-out cross-validation over 40 pelves from the statistical atlas. Figure 6 shows the distributions in positive predictive value (PPV_{A_C}) for the automatically planned accumulation volume for each of the six trajectory types. The results demonstrate >90% overlap between the automatically determined plans and the reference segmentation for most cases. The iliosacral trajectories were the most challenging due to high anatomical variation of the sacral vertebrae among the atlas and larger surface registration error near the sacral foramina, presenting higher likelihood of cortical breach. Still, the iliosacral S1 and S2 trajectories were solved with >80% PPV_{A_C} for all cases.

Figure 6 plots the distance between centerline trajectories in the automatically planned accumulation volume to the bone cortex. Each plot shows three measurements: (i) violin plots (distribution shown in gray for 40 cases) of the distance from the centerline to bone cortex as a function of distance along the trajectory; (ii) the same as (i) but for the cadaver experiment (shown as black curves); and (iii) lower thresholds marked by red horizontal lines at 1.6 mm (typical K-wire radius) and 0 mm (below which the trajectory has breached cortical bone). The average distance from trajectory to cortex was 5.4 mm for AIIS to PSIS 5.1 mm for iliac crest, 3.7 mm for superior ramus, 6.5 mm for posterior column, 3.9 mm for iliosacral S1, and 4.1 mm for iliosacral S2, indicating an acceptable trajectory planning accuracy for the majority of cases. A small number of outliners (1–2 each) was observed for the superior ramus, iliosacral S1, and iliosacral S2 trajectories due to larger surface registration error associated with these trajectory corridors.

The sensitivity of trajectory planning to the accuracy of atlas-to-image registration is analyzed in figure 7 for the superior pubic ramus and iliosacral S1 trajectories. In each case, trajectory conformance (PPV) is shown as a function of registration accuracy by

stopping the algorithm at the Initialization, 4×, 2×, 1×, and FFD steps of the multiresolution schedule. The PPV is seen to improve monotonically at each stage due to better alignment of the SSM on the CT image. The FFD stage significantly improved PPV (student t-test $p < 0.05$), particularly where ASM failed to accurately capture regions of strong shape curvature or strong population variation. To achieve PPV > 0.90, the FFD refinement was required, bringing atlas-to-CT surface RMSE below 2.0 mm. For trajectories in more homogenous regions (e.g. AIIS to PSIS and posterior column trajectories) that are accurately registered by ASM alone, the effect of the FFD refinement was less significant.

Figure 8 shows registered acceptance corridors with respect to the pelvis anatomy for an example atlas member. The left image in each case shows the 3D rendering of the planned trajectory volume ($A_c > 0.5$) overlaid on the 3D surface mesh of the pelvis. The automatically determined trajectory volumes accurately conformed within most of the pelvic volume without breaching cortex. However, the narrow bone corridors (e.g. the superior pubic ramus and S1/S2 sacral bodies) traversed by some trajectories were more prone to misregistration—e.g. intersection of two sides of the corridors as shown in figure 5(b), resulting in a few trajectory outliers. The right image in figure 8 shows the PA view DRR of the pelvis CT overlaid with the PA projection of the trajectory volume. The DRRs are analogous to fluoroscopy images acquired during surgery, in which the trajectory corridors can be challenging to determine in the projection of such complex anatomy. Projection of the trajectory volumes on the DRRs provide an example form of augmented projection imaging demonstrated in the next section.

3.3. Cadaver study: 3D–2D registration accuracy

Figure 8 summarizes the accuracy of 3D–2D registration of preoperative CT to single (PA or LAT) intraoperative radiographs in the cadaver study. Registration performance was evaluated in terms of the PDE and error in 6-DOF transformation, T_{CT}. Figures 8(a) and (b) shows example PA and LAT radiographs overlaid with (blue) Canny edges from DRRs of the CT after 3D–2D registration. The example images were acquired at intermediate steps in inserting K-wires along AIIS to PSIS iliac crest (left), superior ramus (left), and iliosacral (at S1) (tipped marked by arrow). Despite the mismatch in image content between preoperative CT and intraoperative radiographs with a high density of high-contrast instrumentation, pelvic anatomy was fairly well aligned in all views. For calculation of PDE, target points are labeled as white and blue crosses in radiographs and 3D projection from the CT, yielding overall median PDE of 2.1 mm (0.3 mm IQR) after registration. A substantial component of this error is attributed to the challenge in landmark localization (i.e. truth definition), especially in LAT views in which landmarks were difficult to visualize. Landmarks localization exhibited intra-observer precision of 1.98 ± 1.95 mm (single observer repeating three times), and inter-observer precision of 4.37 ± 3.30 mm (three observers repeating three times).

The error in the 3D transformation is shown in figures 9(c) and (d). The errors in (x, y) refer to displacements in the plane of the x-ray detector, and errors in (z) refer to out-of-plane errors (i.e. direction from the detector to the x-ray source). Errors in (z) correspond to a magnification error in the projection geometry of the DRR, which is fairly insensitive with

respect to augmentation of the (x, y) fluoroscopic view. Considering the system geometry used in this work (source to detector distance ~1200 mm and magnification of 1.80), for example, a 5 mm error in z corresponds to a 0.7% change in magnification. In-plane translational error was within ~2 mm, and although out-of-plane translational errors were higher (up to ~6 mm), the associated error in the radiographic plane is small due to magnification. Similarly, rotational errors within the plane of the detector (α) were low (median 0.02°) and higher out-of-plane (β, γ), ~4°. The LAT radiographs yielded higher error in (z) compared to PA or inlet views, because the lower level of image quality (increased attenuation) further challenged the definition of ground truth landmarks.

3.4. Cadaver study: augmented fluoroscopic guidance

Figure 10 illustrates the augmentation of PA and LAT radiographs with acceptance corridors during placement of four K-wires at intermediate steps of insertion. Projection of the trajectory accumulation volumes (P_{A_c}, shown in green) are overlaid onto each radiograph for a given trajectory, providing a quick check on safe bone corridors for the corresponding K-wire. The projection of P_{A_c} is shown in a green colormap with brighter intensity indicating higher confidence in the safety of instrument placement (proportional to the value of the P_{A_c}). Visualization in two views (e.g. PA, LAT, inlet, and/or outlet) provides quick validation of conformance in 3D, potentially reducing guesswork in image interpretation and trial and error in K-wire placement. Among the four trajectories, three of the K-wires (AIIS to PSIS iliac crest, iliosacral S1) are seen to reside entirely within the green acceptance regions, whereas a (purposely) misplaced K-wire in the superior ramus shows a risk of breach if advanced along its current trajectory (figure 9(b)). Manual reference definitions of trajectory contours were highlighted in yellow, showing consistent overlap with P_{A_c}.

The accuracy of augmented fluoroscopic guidance was evaluated in terms of the positive predictive value (PPVP) of the projected accumulation, representing the amount of overlap between the normalized projection accumulation P_{A_c} above 0.5 and the manually defined trajectory contour in the fluoroscopic image plane. As shown in table 2, the PPV$_P$ achieved >95% in AIIS to PIIS and iliosacral S1 trajectory and >90% in superior pubic ramus and iliac crest trajectory, indicating accurate overlap of the projected plans with the reference trajectory corridors. The much narrower bone corridors associated with the superior pubic ramus and iliac crest trajectory contributed to the slightly lower PPV$_P$.

The errors in 3D–2D registration described in section 3.3 propagate to the augmented fluoroscopy scene, where the in-plane error (x, y, α) lead to a change in the translation and orientation of the projected accumulation with respect to the reference definition. Similarly, out-of-plane errors in (z) lead to an apparent change in the size of the projected volume. As shown in figure 9(c), the higher errors in (z) were evident in LAT views in figure 9, where the projected P_{A_c} shown in green are slightly magnified compared to the reference definition. However, the majority of the P_{A_c} was inside the reference definition, and areas extending slightly outside the reference definition contour were of lower value, indicating reduced certainty of safety conformance.

Computation time is another important criterion for application in intraoperative guidance. Table 3 summarizes computation times for each step of the preoperative and intraoperative

steps in the process. Preoperative runtime (ASM, FFD, and trajectory registration to patient-specific CT) was ~9 min in total, which does not bear on intraoperative workflow—a planning step conducted prior to the case. Intraoperative runtime consists of 3D–2D initialization, 3D–2D registration, and augmentation/overlay. For registration of the first fluoroscopic image acquired in the procedure, initialization time is 12.8 ± 3.2 s. For successive fluoroscopic images, the previous registration can be used as an accurate initialization, reducing the 3D–2D registration runtime to 5.0 ± 2.1 s (for initialization within a few mm of the solution). Augmentation/overlay of the fluoroscopic image requires just 0.2 ± 0.1 s. It is worth noting that fluoroscopically guided orthopaedic surgery often relies on step-and-shoot workflow (see continuous fluoroscopy) in which surgeons acquire a single fluoroscopic view ('fluoro shot') that is used to assess anatomy and implant location before advancing the surgical instrument and acquiring a subsequent fluoro shot. Therefore, the tolerable runtime in step-and-shoot guidance is likely ~3–10 s between fluoro shots. The runtimes reported above and in table 3 correspond to a basic research implementation on single GPU using Python and CUDA, and further optimization and/or hardware acceleration is anticipated to bring runtimes in line with workflow requirements. Eventual development of a clinical system should also recognize other important potential factors of latency, including data transfer (2D or 3D images) between the imaging system, registration computer, and display.

4. Discussion and conclusions

A system for automatic trajectory planning and augmented fluoroscopic guidance of percutaneous screw placement in pelvic trauma surgery was reported. The system involves deformable registration of an atlas of pelvic shapes to a patient's (segmentation-free) preoperative CT using ASM registration refined by FFD. The atlas—including 40 segmented CT images of the pelvis, the corresponding ASM, and expert definition of pertinent K-wire trajectory volumes—are available in the public domain at: https://istar.jhu.edu/downloads/.

Experiments demonstrated surface registration accuracy of 1.8 mm in cross-validation and 1.6 mm in a cadaver study. Surgical trajectories are then automatically determined in the patient CT by transforming an atlas of trajectory acceptance corridors via the same registration. The trajectory plans can be overlaid on intraoperative fluoroscopy via 3D–2D registration, showing mean PDE ~2.0 mm and runtime ~12 s in the current work.

The resulting augmentation provides an accurate means of image interpretation and a potentially valuable form of decision support for fluoroscopic guidance of K-wire placement. Because the system uses images already acquired within routine workflow of fluoroscopically guided procedures (and does not introduce the need for additional tracking hardware), it has the potential for mainstream utilization in trauma surgery, where the use of tracking systems is relatively uncommon. The system has the potential to reduce fluoroscopy time and radiation dose by reducing trial-and-error in K-wire placement. Feedback from the trauma surgeon performing the K-wire insertions identified scenarios in which K-wire localization was particularly challenging and the extent to which augmented fluoroscopy helped to resolve uncertainty.

The current work is not without limitations. The ASM was susceptible to registration error in areas of high curvature and foramina, but the surface error tended to be low in areas near the trajectory corridors. Outliers were still observed in the study, however, such as surface intersection in cases of an extremely narrow superior pubic ramus and surface latching onto neighboring structures (e.g. at the femoral head near the acetabulum or lumbar vertebrae near the sacrum endplates). Methods have been proposed to resolve such challenges in ASM, including expanding the 1D search space along surface normal to an omnidirectional space (Kainmueller et al 2013), adopting a hierarchical SSM for more robust registration (Cerrolaza et al 2012), and using a more advanced graph-cut optimization for vertex location adjustment (Seim et al 2008). Extension of the current automatic planning system to these methods merits future investigation. The method for trajectory planning is relatively insensitive to such errors, since the interior regions associated with the acceptance corridors (computed by MVC interpolation) is relatively robust against localized surface registration error.

The trajectory planning was based on accumulation of annotated trajectory volumes from all atlas members, which is comparable to the majority voting scheme widely used in deformable image registration-based multi-atlas segmentation (Heckemann et al 2006, Aljabar et al 2009). It has the advantages of incorporating anatomical variations across the atlas members and reducing bias toward a single atlas member, resulting in more accurate and more robust trajectory planning, particularly for a sufficiently large atlas. Recent work in direct image-based multi-atlas segmentation and label fusions have shown that more sophisticated weighting schemes can be used to improve algorithm accuracy (Artaechevarria et al 2009, Sdika 2010), where weights are assigned to atlas members based on registration quality. Such ideas can potentially be translated to the current framework in which each atlas member’s accumulation is weighted by its similarity to the patient shape. Future work will investigate such weighting to potentially improve trajectory planning.

The image-to-radiograph 3D–2D registration method provided accurate patient registration (<2 mm) of the preoperative CT image and individual fluoroscopy images acquired in routine clinical workflow. The method was implemented on GPU, yielding ~13 s computation time for each registration. Reducing computation time is still desirable for more real-time fluoroscopic image update and merits future work. For example, we are considering improving the level of parallelization in the 3D–2D registration, using better initialization method by incorporating the C-arm gantry encoder, and more time-efficient optimization method. (Goerres et al 2017b) proposed a deformable known component 3D–2D registration to locate K-wires in 3D space using multiple radiographs. Such a method can certainly be incorporated within the proposed system workflow as a form of 3D navigation (i.e. visualization with respect to the preoperative 3D image). On the other hand, atlas-to-image registration and automatic trajectory planning were currently implemented on CPU, yielding ~3 min and ~9 min respectively. For translation to trauma surgery scenarios with rapid workflow requirements, further acceleration is desirable and may be feasible using a sparser representation of the dense accumulation map or a parallelized implementation on GPU. Previous research has also shown the possibility of 3D–2D registration that relates radiographs directly to a 3D deformable statistical model (Sadowsky et al 2007, Ehlke et al

2013), which can potentially avoid computation time on surface registration and planning, and deserves future investigation.

The current atlas contains six categories of clinically relevant trajectories (AIIS to PSIS, superior pubic ramus, iliac crest, posterior column, and trans-sacral iliosacral S1 and S2)—ten trajectories in total—that cover the majority of percutaneous fixation cases. However, other trajectories can be encountered depending on particular fractures, such as from the AIIS to the iliac crest for lateral compression (Giannoudis et al 2007), which could certainly be added to the atlas. Furthermore, this work only considered trans-iliac trans-sacral iliosacral screws in S1 and S2 levels, which are plausible in normal sacra. In cases of upper sacral dysmorphism that commonly exhibits enlarged sacral foramina and acute alar slope, trans-sacral iliosacral screws are not advisable (Miller and Routt 2012), and a one-sided screw along an oblique pathway may be required. Future investigation could involve differentiating normal from dysmorphic sacra via ASM surface registration and automatically planning oblique trajectories to accommodate such anatomical variations.

The cross-validation and cadaver studies involved reasonably high-quality preoperative CT images that were free of artifact. Other application scenarios may present a challenge to 3D image quality—e.g. intraoperative CBCT images acquired at lower dose (higher noise) with higher levels of artifact and limited field of view. With respect to the automatic planning method described above, the ASM surface registration is attracted to high bone gradients and is relatively insensitive to low-frequency artifacts (e.g. cupping and shading artifacts)—e.g. related to elevated levels of x-ray scatter in CBCT. The principal component constraints regularization in surface registration is also robust to high-frequency artifacts (e.g. streaking and ring artifacts). The surface registration has also been shown to be robust to noise in low-dose CBCT (Vijayan et al 2019), where ASM was found to perform comparably over a dose range ~15–35 mGy in registering the lumbar spine. With respect to 3D–2D registration and augmented fluoroscopic guidance, the GO similarity metric and evolution-based optimization have been shown to be robust to content mismatch (e.g. surgical tools and implants) (De Silva et al 2016), and the robustness to mismatch may be similarly important to mitigate the effect of high-frequency CBCT artifacts, such as metal artifacts and streaking. Quantitative analysis of the performance of the planning and guidance methods over a broad range in CT and CBCT image quality is the subject of future investigation.

In conclusion, we have proposed a system for automatic surface registration, trajectory planning, and augmented fluoroscopic guidance for percutaneous fixation in pelvic trauma surgery. The accuracy and reliability of the system demonstrated in this work provides important quantitation of accuracy and feasibility in support of future clinical pilot studies in orthopaedic surgery.

Acknowledgments

This research was supported by NIH grant R01-EB-017226. Academic industry partnership is gratefully acknowledged with Siemens Healthineers (Erlangen Germany) on mobile C-arm imaging and Medtronic (Littleton MA) on O-arm imaging and registration. Thanks to Ben Ramsay for segmenting the CT images in the atlas.

References

Aljabar P, Heckemann RA, Hammers A, Hajnal JV and Rueckert D 2009 Multi-atlas based segmentation of brain images: atlas selection and its effect on accuracy NeuroImage 46 726–38 [PubMed: 19245840]

Artaechevarria X, Munoz-Barrutia A and Ortiz-de-Solorzano C 2009 Combination strategies in multi-atlas image segmentation: application to brain MR data IEEE Trans. Med. Imaging 28 1266–77 [PubMed: 19228554]

Banerjee S, Starr AJ and Banerjee R 2016 Computed tomography-based software safely guides anterograde percutaneous anterior and posterior column acetabular screws J. Surg. Orthop. Adv 25 80–5 [PubMed: 27518290]

Bishop JA and Routt ML Jr 2012 Osseous fixation pathways in pelvic and acetabular fracture surgery: Osteology, radiology, and clinical applications J. Trauma Acute Care Surg. 72 1502 [PubMed: 22695413]

Buls N, Pagés J, de Mey J and Osteaux M 2003 Evaluation of patient and staff doses during various CT fluoroscopy guided interventions Health Phys. 85 165–73 [PubMed: 12938963]

Clark K, Vendt B, Smith K, Freymann J, Kirby J, Koppel P, Moore S, Phillips S, Maffitt D, Pringle M, Tarbox L and Prior F 2013 The Cancer Imaging Archive (TCIA): Maintaining and Operating a Public Information Repository J. Digit. Imaging 26 1045–57 [PubMed: 23884657]

Cerrolaza JJ, Villanueva A and Cabeza R 2012 Hierarchical statistical shape models of multiobject anatomical structures: application to brain MRI IEEE Trans. Med. Imaging 31 713–24 [PubMed: 22194238]

Cootes TF, Taylor CJ and Lanitis A 1994 Active Shape Models: Evaluation of a Multi-Resolution Method for Improving Image Search Proc. of the British Machine Conf. (Colchester: BMVA Press) pp 32.1–32.10

De Silva T, Uneri A, Ketcha MD, Reaungamornrat S, Kleinszig G, Vogt S, Aygun N, Lo S-F, Wolinsky J-P and Siewerdsen JH 2016 3D–2D image registration for target localization in spine surgery: investigation of similarity metrics providing robustness to content mismatch Phys. Med. Biol. 61 3009–25 [PubMed: 26992245]

Ehlke M, Ramm H, Lamecker H, Hege H-C and Zachow S 2013 Fast generation of virtual x-ray images for reconstruction of 3D anatomy IEEE Trans. Vis. Comput. Graph 19 2673–82 [PubMed: 24051834]

Ellingsen LM, Chintalapani G, Taylor RH and Prince JL 2010 Robust deformable image registration using prior shape information for atlas to patient registration Comput. Med. Imaging Graph 34 79–90 [PubMed: 19515532]

Giannoudis PV, Tzioupis CC, Pape H-C and Roberts CS 2007 Percutaneous fixation of the pelvic ring J. Bone Joint Surg. Br 89 145–54 [PubMed: 17322425]

Goerres J et al. 2017a Planning, guidance, and quality assurance of pelvic screw placement using deformable image registration Phys. Med. Biol 62 9018–38 [PubMed: 29058687]

Goerres J et al. 2017b Spinal pedicle screw planning using deformable atlas registration Phys. Med. Biol 62 2871 [PubMed: 28177300]

Gras F, Marintschev I, Wilharm A, Klos K, Mückley T and Hofmann GO 2010 2D-fluoroscopic navigated percutaneous screw fixation of pelvic ring injuries—a case series BMC Musculoskeletal Disorders 11 153 [PubMed: 20609243]

Hansen N, Müller SD and Koumoutsakos P 2003 Reducing the time complexity of the derandomized evolution strategy with covariance matrix adaptation (CMA-ES) Evolutionary Comput. 11 1–18

Heckemann RA, Hajnal JV, Aljabar P, Rueckert D and Hammers A 2006 Automatic anatomical brain MRI segmentation combining label propagation and decision fusion NeuroImage 33 115–26 [PubMed: 16860573]

Isgum I, Staring M, Rutten A, Prokop M, Viergever MA and van Ginneken B 2009 Multi-atlas-based segmentation with local decision fusion—application to cardiac and aortic segmentation in CT scans IEEE Trans. Med. Imaging 28 1000–10 [PubMed: 19131298]

Ju T, Schaefer S and Warren J 2005 Mean value coordinates for closed triangular meshes ACM SIGGRAPH 2005 Papers SIGGRAPH ‘05 (New York: ACM) pp 561–6

Kainmueller D, Lamecker H, Heller MO, Weber B, Hege H-C and Zachow S 2013 Omnidirectional displacements for deformable surfaces Med. Image Anal 17 429–41 [PubMed: 23523192]

Knez D, Likar B, Pernuš F and Vrtovec T 2016 Computer-assisted screw size and insertion trajectory planning for pedicle screw placement surgery IEEE Trans. Med. Imaging 35 1420–30 [PubMed: 26742125]

Lamecker H, Seebass M, Hege H-C and Deuflhard P 2004 A 3D statistical shape model of the pelvic bone for segmentation Proc. SPIE 5370 1341

Lee K, Lee KM, Park MS, Lee B, Kwon DG and Chung CY 2012 Measurements of surgeons' exposure to ionizing radiation dose during intraoperative use of C-arm fluoroscopy Spine 37 1240–4 [PubMed: 22198350]

Loisel F, Menu G, Boyer E, Pluvy I and Obert L 2017 Radiation exposure and the orthopedic surgeon's hand: measurement of the equivalent dose over 13 months Hand Surg. Rehabil 36 97–101 [PubMed: 28325434]

Lorenzo-Valdés M, Sanchez-Ortiz GI, Mohiaddin R and Rueckert D 2002 Atlas-based segmentation and tracking of 3D cardiac MR images using non-rigid registration Medical Image Computing and Computer-Assisted Intervention—MICCAI 2002 (Lecture Notes in Computer Science) ed Dohi T and Kikinis R (Berlin: Springer) pp 642–50

Miller AN and Routt MLC 2012 Variations in sacral morphology and implications for iliosacral screw fixation J. Am. Acad. Orthop. Surg 20 8–16 [PubMed: 22207514]

Myronenko A and Song X 2010 Point set registration: coherent point drift IEEE Trans. Pattern Anal. Mach. Intell 32 2262–75 [PubMed: 20975122]

Otake Y, Wang AS, Webster Stayman J, Uneri A, Kleinszig G, Vogt S, Khanna AJ, Gokaslan ZL and Siewerdsen JH 2013 Robust 3D–2D image registration: application to spine interventions and vertebral labeling in the presence of anatomical deformation Phys. Med. Biol 58 8535–53 [PubMed: 24246386]

Ren L, Zhang Y and Yin F 2014 A limited-angle intrafraction verification (LIVE) system for radiation therapy Med. Phys 41 020701 [PubMed: 24506590]

Roth HR, Lu L, Seff A, Cherry KM, Hoffman J, Wang S, Liu J, Turkbey E and Summers RM 2014 A new 2.5D representation for lymph node detection using random sets of deep convolutional neural network observations Medical Image Computing and Computer-Assisted Intervention–MICCAI 2014 vol 8673 pp 520–7

Routt ML, Simonian PT and Grujic L 1995 The retrograde medullary superior pubic ramus screw for the treatment of anterior pelvic ring disruptions: a new technique J. Orthop. Trauma 9 35–44 [PubMed: 7714652]

Sadowsky O, Chintalapani G and Taylor RH 2007 Deformable 2D–3D registration of the pelvis with a limited field of view, using shape statistics Medical Image Computing and Computer-Assisted Intervention—MICCAI 2007 (Lecture Notes in Computer Science) ed Ayache N et al. (Berlin: Springer) pp 519–26

Schildhauer TA, McCulloch P, Chapman JR and Mann FA 2002 Anatomic and radiographic considerations for placement of transiliac screws in lumbopelvic fixations J. Spinal Disord. Tech 15 199–205 [PubMed: 12131419]

Sdika M 2010 Combining atlas based segmentation and intensity classification with nearest neighbor transform and accuracy weighted vote Med. Image Anal 14 219–26 [PubMed: 20056473]

Seff A, Lu L, Cherry KM, Roth H, Liu J, Wang S, Hoffman J, Turkbey EB and Summers RM 2014 2D View aggregation for lymph node detection using a shallow hierarchy of linear classifiers (arXiv:1408.3337)

Seim H, Kainmueller D, Heller M, Lamecker H, Zachow S and Hege H-C 2008 Automatic segmentation of the pelvic bones from CT data based on a statistical shape model Proc. of the First Eurographics Conf. on Visual Computing for Biomedicine EG VCBM'08 (Aire-la-Ville: Eurographics Association) pp 93–100

Starr AJ, Reinert CM and Jones AL 1998 Percutaneous fixation of the columns of the acetabulum: a new technique J. Orthop. Trauma 12 51–8 [PubMed: 9447519]

Vijayan R, De Silva T, Han R, Uneri A, Doerr S, Ketcha M, Perdomo-Pantoja A, Theodore N and Siewerdsen J 2019 Automatic trajectory and instrument planning for robot-assisted spine surgery Proc. SPIE 10951 1095102

Yoshihara H and Yoneoka D 2014 Demographic epidemiology of unstable pelvic fracture in the United States from 2000 to 2009: trends and in-hospital mortality J. Trauma Acute Care Surg 76 380–5 [PubMed: 24398776]

Zhang J, Fernandez J, Hislop-Jambrich J and Besier TF 2016 Lower limb estimation from sparse landmarks using an articulated shape model J. Biomech 49 3875–81 [PubMed: 28573974]

Zhang Y, Yin F, Segars W and Ren L 2013 A technique for estimating 4D-CBCT using prior knowledge and limited-angle projections Med. Phys 40 121701 [PubMed: 24320487]

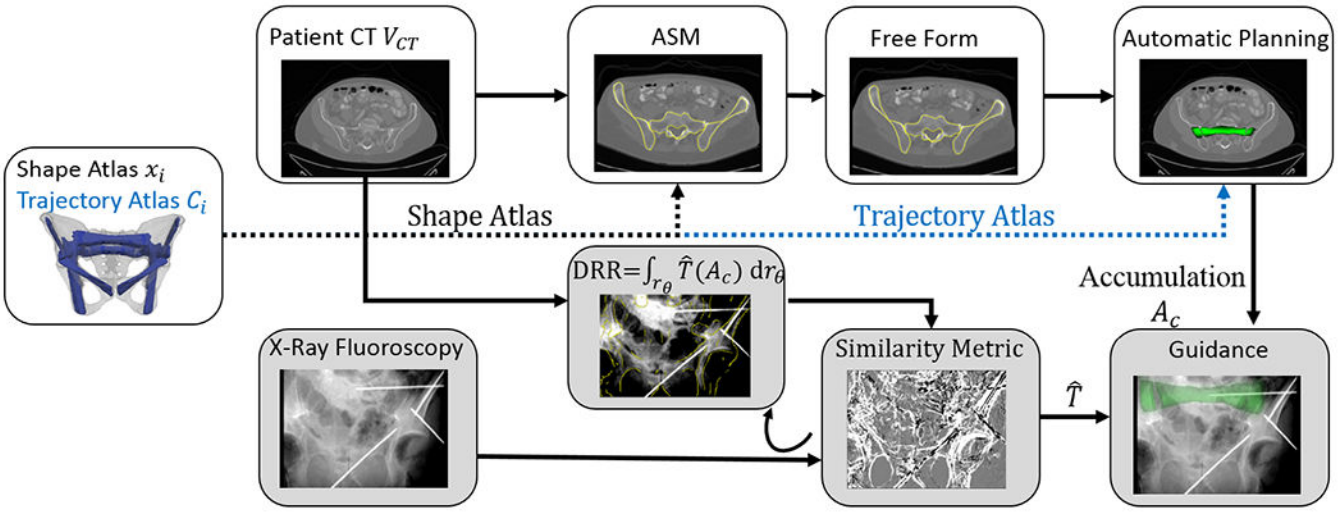

Figure 1.

Flowchart for automatic trajectory planning and augmented fluoroscopy for guidance of pelvic trauma surgery, illustrating preoperative (top row) and intraoperative (bottom row) registration steps.

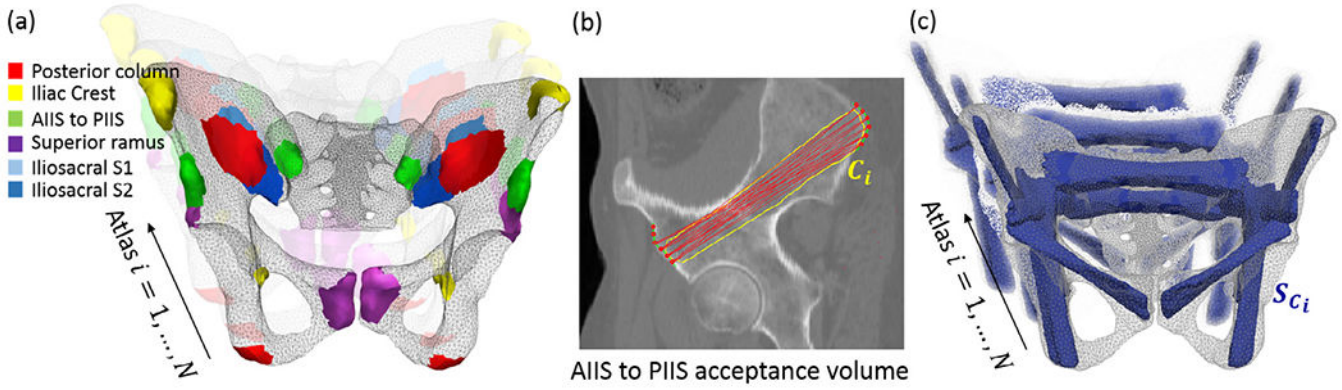

Figure 2.

Atlas of volumetric reference trajectories (acceptance corridors) in pelvic trauma surgery. (a) Manually annotated trajectory entry regions. (b) Example view of permissible AIIS trajectories (red) connecting two entry surfaces to generate a volumetric acceptance corridor, C_i (yellow contour). (c) Example reference acceptance corridor meshes, S_{C_i} (blue). The current atlas comprised 40 pelves, each with ten reference trajectory volumes, and made available in the public domain.

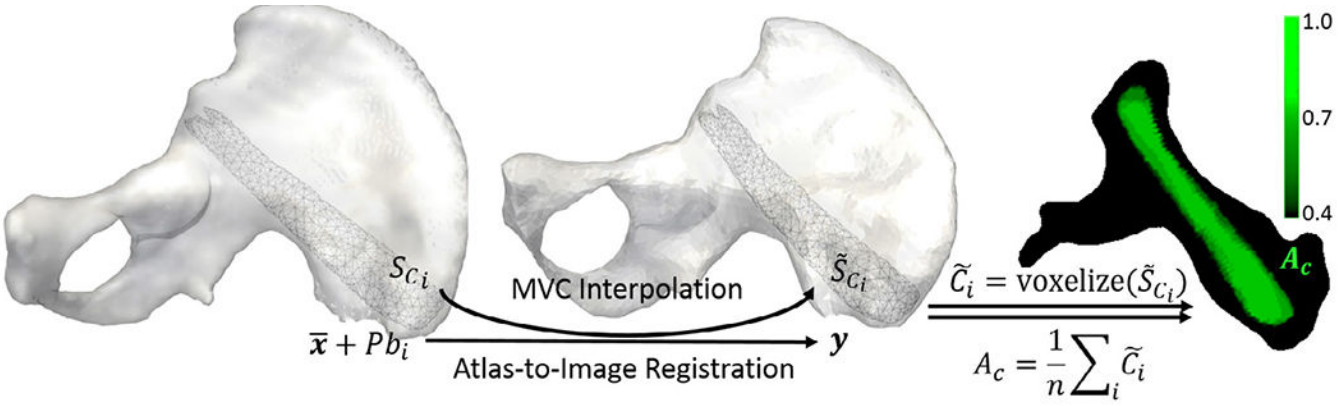

Figure 3.

Automatic definition of pelvic screw trajectory. Acceptance corridor surfaces S_{C_i} from atlas members are mapped to the patient $\tilde{S}_{C_i}$ via the transformation obtained by the atlas-to-image registration using MVC interpolation. The normalized summation of voxelizations of the mapped acceptance corridors of all atlas members yields an accumulation map A_c.

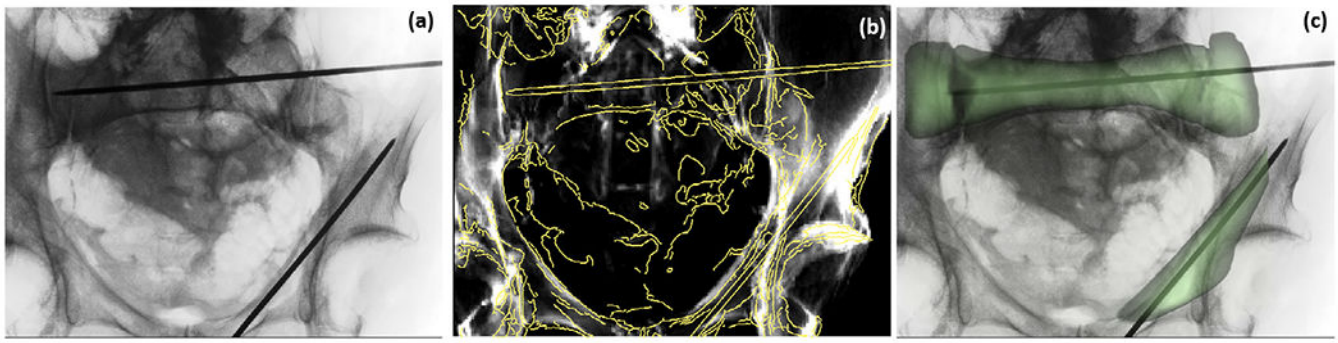

Figure 4.

Augmented fluoroscopic guidance. (a) Inlet view of the pelvis showing a superior ramus and iliosacral S1 K-wire insertion. (b) DRR of preoperative CT after 3D–2D registration, showing close alignment with the fluoroscopic view, represented by Canny edges of the projection in (a). (c) Projection of the trajectory accumulation A_c onto the fluoroscopy image using the resulting 3D–2D registration. Augmentation of the fluoroscopic scene with such acceptance trajectories aids interpretation of complex 3D relationships of pelvic morphology and device orientation in the 2D projection view. In two fluoroscopic views (inlet and outlet, for example), conformance of the K-wire within augmented regions provides quick validation of conformance within the acceptance corridor.

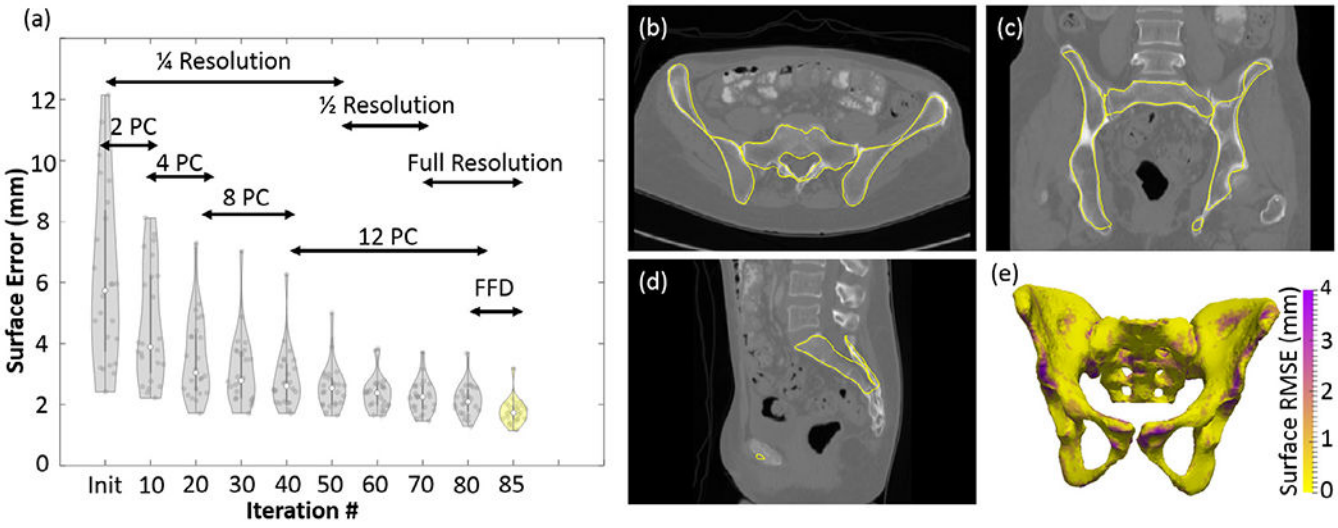

Figure 5.

Accuracy of 3D atlas registration. (a) Surface RMSE measured as a function of iteration # over the course of a multiresolution pyramid in image resolution (binning 4–1×) and number of principal components (2–12). Further improvement in registration accuracy was obtained using FFD at the final stage. (b)–(d) Axial, sagittal, and coronal views of a CT image of a cadaver overlaid with the registered atlas model (yellow). (e) 3D rendering of the pelvis, where the color of each surface vertex encodes surface distance error.

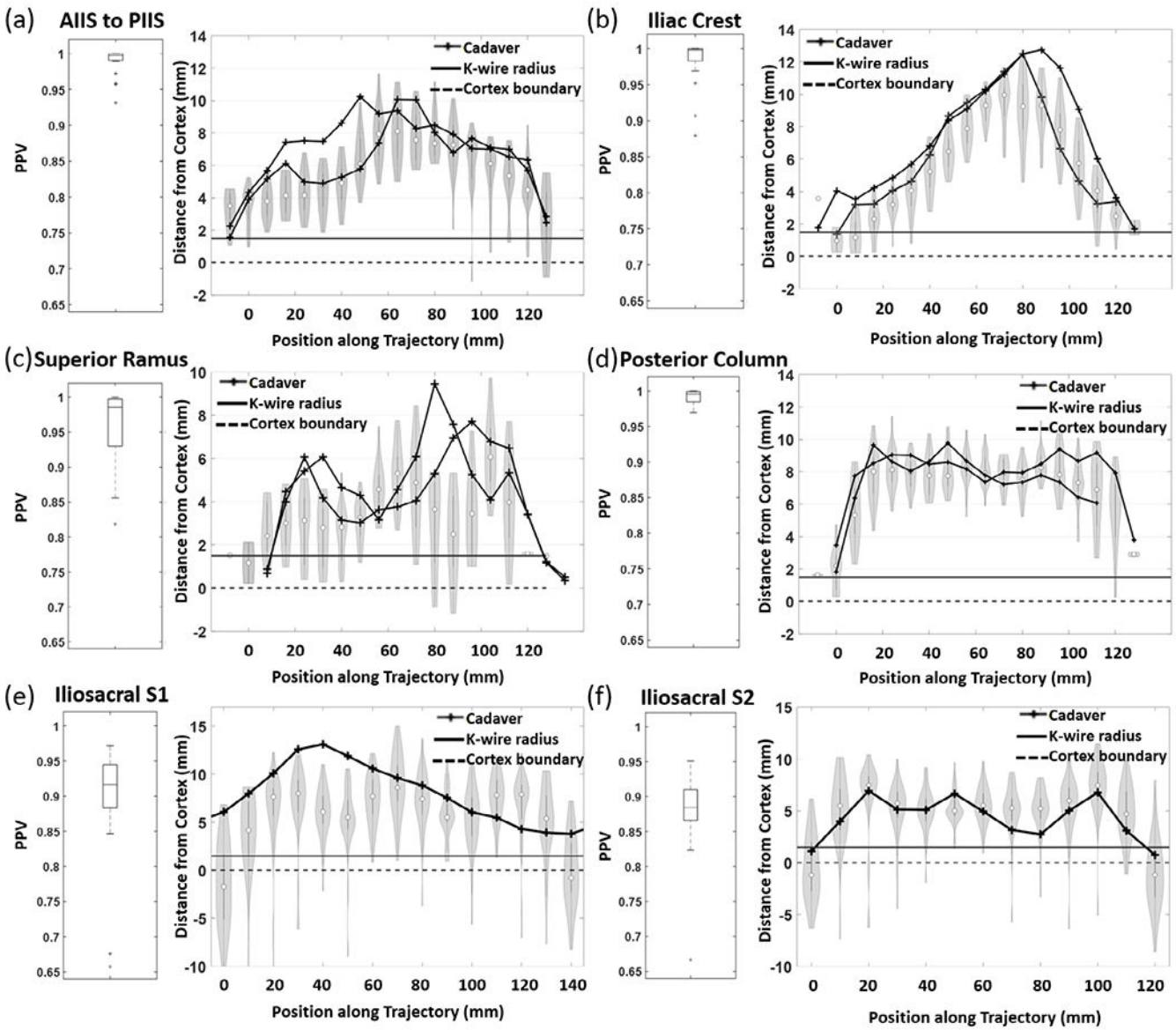

Figure 6.

Accuracy of automatic planning. In each case, the boxplot at left shows the distribution in PPV of the computed acceptance corridor compared to the reference. Plots in the right of each case show distributions in the distance between the centerline trajectory and the bone cortex as a function of distance along the planned trajectory. Solid black lines are for the cadaver experiment. Horizontal solid and dashed lines indicate 1.6 mm (K-wire diameter) and 0.0 mm from the cortex boundary below which the distance is indicative of breach. The endpoints of each plot represent the entry and endpoint of trajectories at the cortical surface.

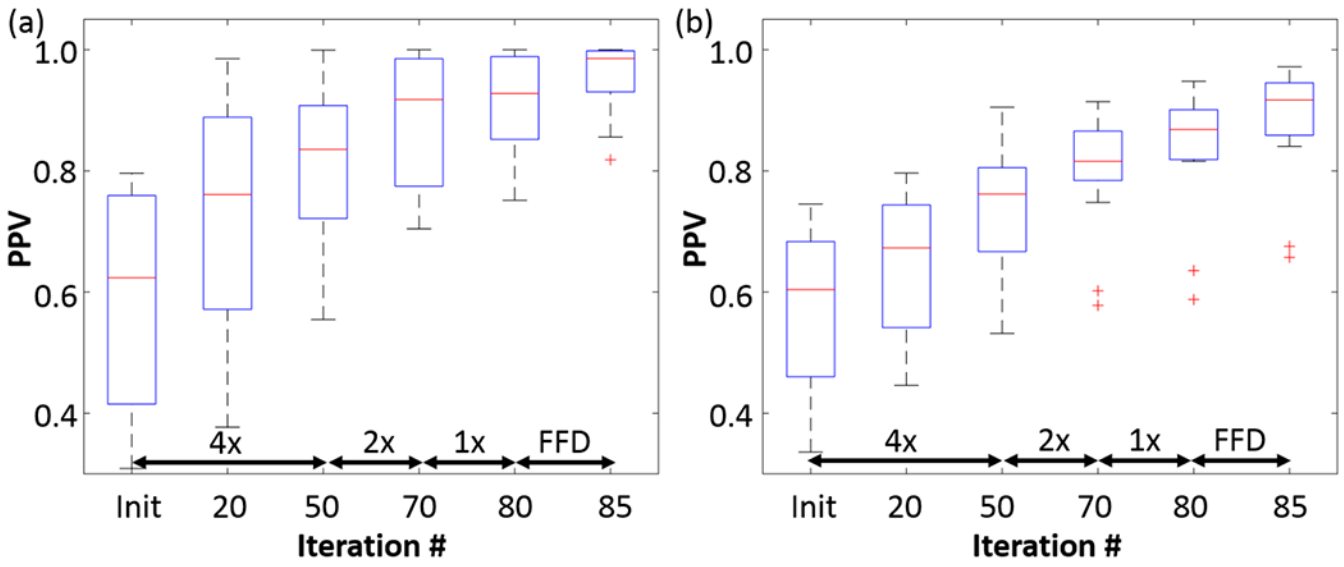

Figure 7.

Sensitivity of trajectory planning to the accuracy of atlas-to-image registration. (a) Superior ramus trajectory. (b) Iliosacral S1 trajectory. In each case, the boxplot shows the distribution in PPV of the computed acceptance corridor compared to the reference.

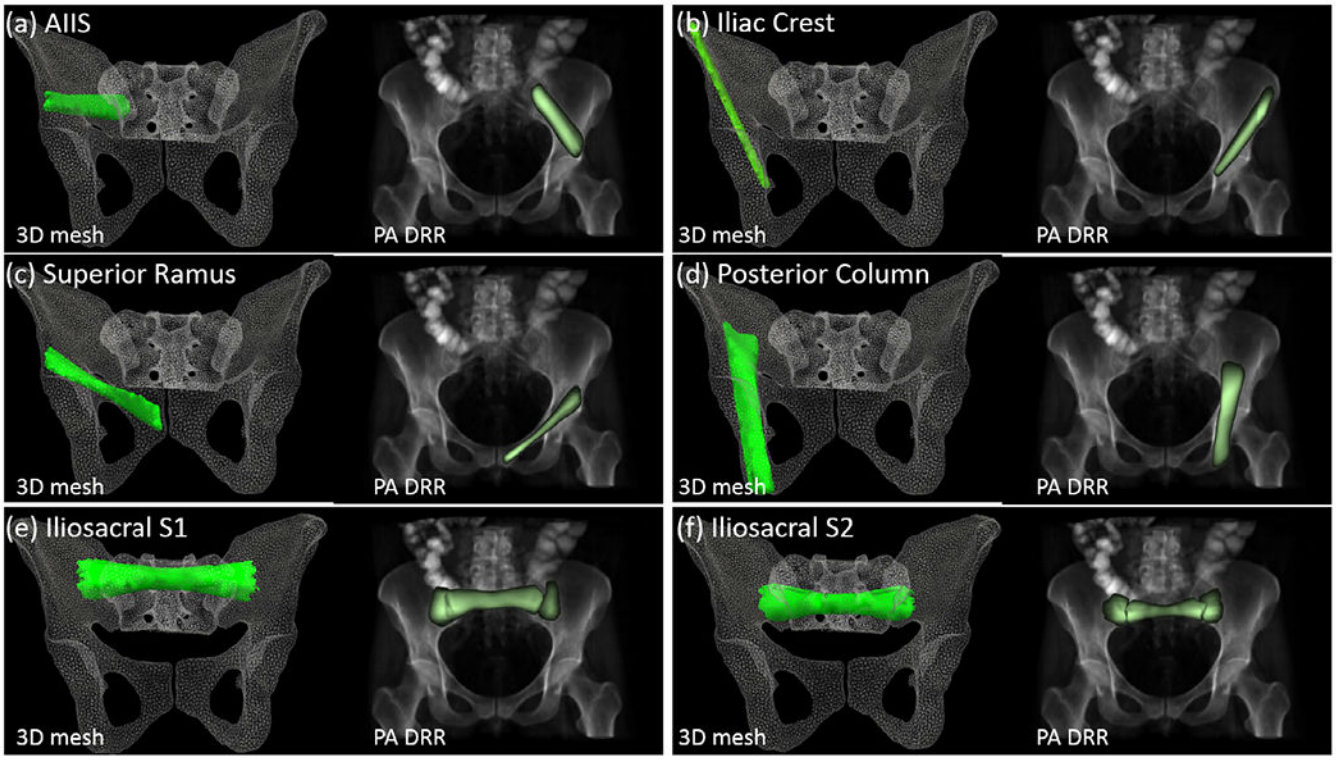

Figure 8.

Automatic planning of six example trajectories in pelvic trauma surgery: (a) AIIS, (b) iliac crest, (c) superior ramus, (d) posterior column, and iliosacral (e) S1 and (f) S2. Images on the left in each case show 3D visualization of the pelvis surface mesh after surface-to-image registration with automatically planned 3D accumulation volume (green). Images on the right in each case show a PA DRR overlaid with projected accumulation volume (green).

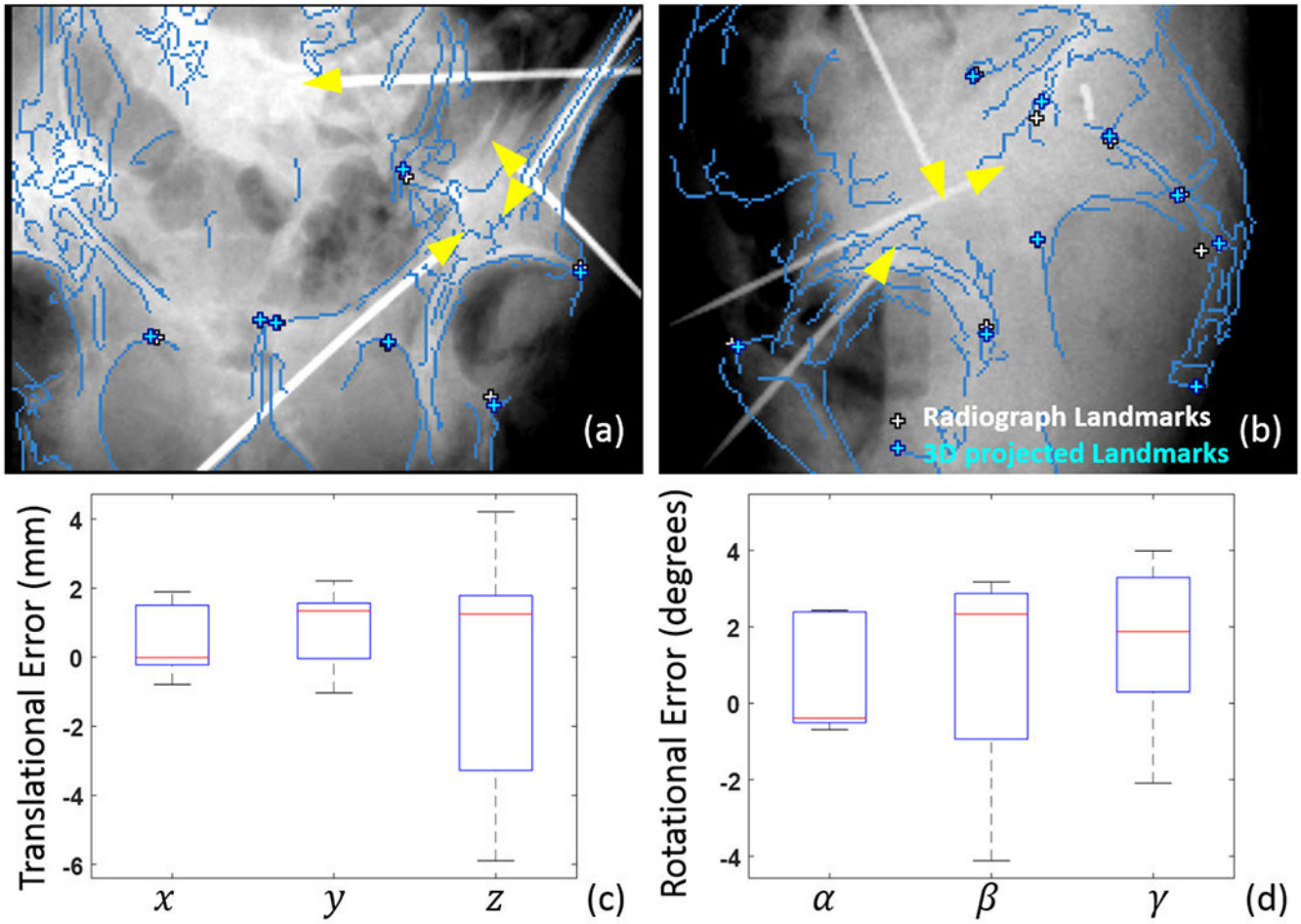

Figure 9.

3D–2D registration accuracy in cadaver studies. Example (a) PA and (b) LAT radiographs overlaid with Canny edges of the registered DRR. Anatomical landmarks defined in the radiographs are labeled in white, and those projected from CT are shown in blue. Yellow arrows depict the tips of each K-wire. (c) Translational and (d) rotational error in the 3D–2D registration transformation. Note that (x, y) and α refer to in-plane displacements and rotation, respectively, whereas z and (β, γ) refer to out-of-plane translation and rotations.

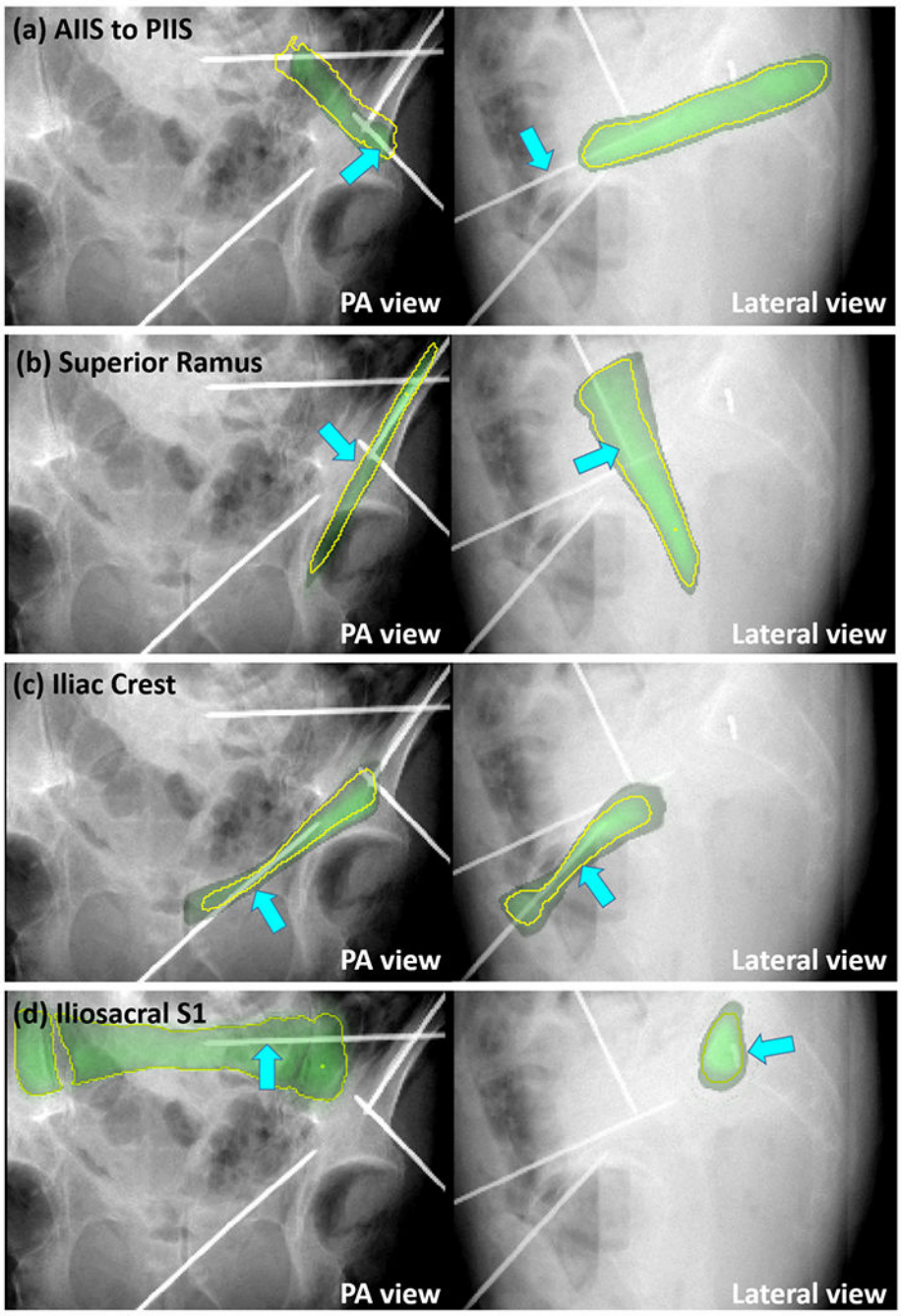

Figure 10.

Augmented fluoroscopy in the cadaver study. Projection of automatic planning trajectories (green) of four cases of K-wire placement: (a) AIIS to PSIS (b) superior ramus, (c) iliac crest, and (d) iliosacral at S1. Each superimposes the projected acceptant volume on PA and LAT radiographs via 3D–2D registration. Reference trajectory boundaries $P_{A_{\text{ref}}}$ are labeled in yellow, and blue arrows point to the pertinent K-wire in each case.

Table 1.

Multiresolution pyramid schedule.

Iteration #	Image binning	Gaussian kernel width (voxels)	# Principal components
10	4×	4	2
20	4×	4	4
30	4×	4	8
40	4×	4	8
50	4×	4	12
60	2×	2	12
70	2×	2	12
80	1×	1	12
85	1×	1	FFD

Table 2.

The PPV_P of projected accumulation in augmented fluoroscopic guidance.

Trajectory	PPV_P
AIIS to PSIS	94.5%
Superior pubic ramus	91.7%
Iliac crest	92.2%
Iliosacral S1	97.4%

Table 3.

Computation time of the preoperative and intraoperative system pipeline.

Preoperative runtime (mean ± std) (s)		**Intraoperative runtime (mean ± std) (s)**	
ASM	40.7 ± 1.8	Initialization	12.8 ± 3.2
FFD	0.7 ± 0.1	3D–2D registration	5.0 ± 2.1
Trajectory planning	490.5 ± 30.0	Fluoroscopic augmentation	0.2 ± 0.1